

Polarization-Tuned Fano Resonances in All-Dielectric Short-Wave Infrared Metasurface

Anis Attiaoui,¹ Gérard Daligou,¹ Simone Assali,¹ Oliver Skibitzki,² Thomas Schroeder,³ and Oussama Moutanabbir¹

¹*Department of Engineering Physics, École Polytechnique de Montréal,
C.P. 6079, Succ. Centre-Ville, Montréal, Québec, Canada H3C 3A7*

²*IHP—Leibniz-Institut für innovative Mikroelektronik, Im Technologiepark 25, 15236 Frankfurt (Oder), Germany*

³*Leibniz-Institut für Kristallzüchtung, Max-Born-Straße 2, 12489 Berlin, Germany*

The short-wave infrared (SWIR) is an underexploited portion of the electromagnetic spectrum in metasurface-based nanophotonics despite its strategic importance in sensing and imaging applications. This is mainly attributed to the lack of material systems to tailor light-matter interactions in this range. Herein, we address this limitation and demonstrate an all-dielectric silicon-integrated metasurface enabling polarization-induced Fano resonance control at SWIR frequencies. The platform consists of a two-dimensional Si/Ge_{0.9}Sn_{0.1} core/shell nanowire array on a silicon wafer. By tuning the light polarization, we show that the metasurface reflectance can be efficiently engineered due to Fano resonances emerging from the electric and magnetic dipoles competition. The interference of optically induced dipoles in high-index nanowire arrays offers additional degrees of freedom to tailor the directional scattering and the flow of light while enabling sharp polarization-modulated resonances. This tunability is harnessed in nanosensors yielding an efficient detection of 10^{-2} changes in the refractive index of the surrounding medium.

Keywords: SWIR, Metasurface, Polarization tunability, Fano resonance, Si/GeSn core/shell, Nanowire, Refractive index sensing

All-dielectric nanostructures are versatile platforms to engineer light-matter interactions and exploit a range of processes including Fano interference [1, 2] and strong coupling [3]. Their fundamental properties support both electric dipole (ED) and strong magnetic dipole (MD) resonances in addition to higher-order multipole resonances, which substitute lossy ohmic currents with low-loss displacement currents emerging from bounded electrons oscillations [1, 4, 5]. This is in contrast to plasmonic particles, where a non-negligible magnetic response can only be achieved using complex geometries [6, 7]. Nonetheless, the widely used materials for metasurfaces still remain radiating metallic antennas [8] despite numerous challenges [9]. For instance, the significant non-radiative conductor losses usually lead to a broad bandwidth (> 50 nm) and restrict the achievable Q -factor to less than ~ 10 [10]. Additionally, the anisotropic electromagnetic response impedes the control of the resonance. In fact, given that metasurface geometrical design influences the spatial overlap of resonance-related field distributions, it becomes challenging to dynamically modulate the resonant features with a fixed design structure.

It is thus highly coveted to develop low-loss resonators made entirely of dielectrics with average permittivity in the $\approx 2 - 14$ range, whilst still being sufficiently subwavelength in the propagation direction. In this regard, a plethora of materials has been explored [11–14] enabling novel photonic functionalities [15–18]. The resonant multipole interplay in all-dielectric metasurfaces can induce sharp features in light reflection and transmission spectra, including Fano resonances [2]. The characteristic asym-

metric Fano line shape is due to the coherent interference between two hybridized broad and narrow scattering pathways [2, 19]. Tuning these resonances mainly rely on changing the asymmetry parameter, the geometry, or the coupling distance within the unit cell of the metasurface [20, 21]. Indeed, current approaches to modulate Fano resonances generally work in passive mode [22]. Therefore, it is critical to establish alternative design routes for active control of metasurfaces. One possibility is to change the incident light polarization to alter the resonance loss [23]. Thus, a dynamic control of resonances can be achieved by rotating the corresponding field nodes of the respective modes to ultimately tune their coupling efficiency.

Herein, we propose a new material system to simultaneously address the aforementioned challenges. This platform leverages the flexibility offered by the emerging silicon-compatible GeSn semiconductors [24] to implement all-dielectric core/shell Si/GeSn base-tapered nanowire (NW)-metasurfaces, where the polarization-modulated response is controlled in the heretofore unexplored SWIR range. By rotating the polarization state of incident light, polarization-induced resonance (PIR) modes are observed and finely controlled with a modulation depth as high as 75%. Furthermore, by combining the narrow Fano resonance linewidth with the strong near-field confinement, we demonstrate a room-temperature optical refractive index (RI) nanosensor operating between 1.6 and 1.9 μm , with a sensitivity as high as 386 nm/RIU and a figure-of-merit (FoM) of 12. The Fano resonance spectral shift is induced by a 10^{-2} change in the properties of the surrounding environment RI.

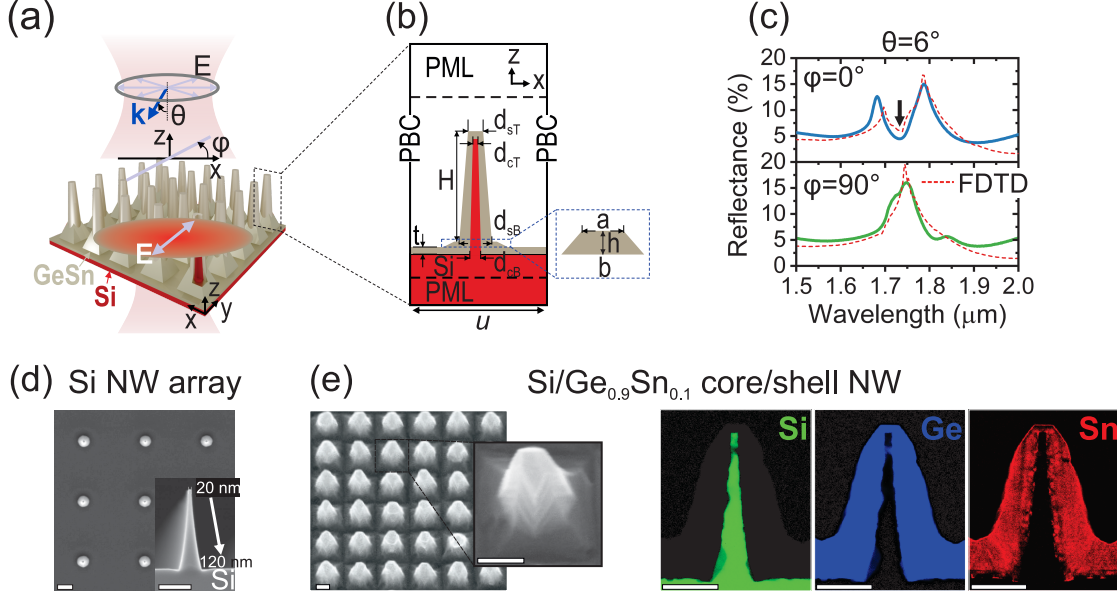


FIG. 1. Configuration of the Si/GeSn NW metasurface allowing polarization-enabled modulation of Fano resonance. (a) 3D schematic of the proposed core/shell array metasurface where the dynamic modulation of the polarization state of the incident light is demonstrated. The polarization and incidence angle, φ and θ , are also shown. (b) The relevant geometrical parameters of the FDTD simulation domain of the tapered NW are indicated: the height H , top shell diameter d_{ST} , bottom shell diameter d_{SB} , top core diameter d_{CT} , bottom core diameter d_{CB} , overgrown GeSn layer t , and top base a , bottom base b and height of the trapezoid H . The geometrical parameters are presented in the Table S4. (c) Measured and FDTD simulated specular reflectance spectra of the Si/GeSn core/shell at two different polarizations ($p \equiv (\varphi = 0^\circ)$ and $s \equiv (\varphi = 90^\circ)$). The black arrow indicates the peak position where the reflectance is suppressed. SEM images (tilting angle of 45°) of (d) the Si core NW template, where the inset indicated the tapered NW geometry. The Si/GeSn core/shell NW images are also shown in panel (e) where the zoom in map highlights the tapered base. The associated individual EELS maps for Si, Ge, and Sn atoms are also shown. The scale bar in all images is fixed to 200 nm.

Design and characterization. The schematic of the designed semiconductor metasurface is shown in Fig. 1a. The unit cell consists of a core/shell Si/Ge_{0.9}Sn_{0.1} tapered NW. The NW dimensions are chosen such that the resonance of both ED and MD modes are closely aligned in frequency. The geometrical configuration of a single unit cell is illustrated in Fig. 1b. Numerical simulations of the fabricated structures are carried out using a 3D finite-difference time domain (FDTD) solver (Methods). The corresponding simulated and measured reflectance spectra are displayed in Fig. 1c for two different incident light polarization (p -type: $\varphi = 0^\circ$, and s -type: $\varphi = 90^\circ$). A distinct PIR-like dip, accompanied with two peaks, is observed at 1734 nm for $\varphi = 0^\circ$. When the electric field is polarized along the z -axis, $\varphi = 90^\circ$, a narrow reflectance peak with a full-width half-maximum (FWHM) of 32 nm appears. The reflectance amplitude decreases from 17% to 5% as φ decreases from 90° to 0° . The measured reflectance is acquired by illuminating the sample with a near-normal incident (6°) broadband white light with a tunable incident light polarization (Methods). Note that the measured specular reflectance of the core/shell array is lower than that of bare Si NW array in the wavelength range between $1.1 \mu\text{m}$ and $2.5 \mu\text{m}$ (Fig. S1). A Ge_{0.9}Sn_{0.1} thin film has an estimated electronic band

gap, of $\sim 0.65 \text{ eV}$ ($\approx 1.9 \mu\text{m}$) [25]. The low reflection can be attributed to light absorption within the array. The reflectance R is low over the whole spectral and angular range, with a maximum reflectance above 13% for $\lambda \geq 2.25 \mu\text{m}$.

The proposed nanostructure (Fig. 1b) is composed of: Si substrate, $\sim 100 \text{ nm}$ -thick GeSn layer, Ge_{0.9}Sn_{0.1} trapezoidal base, tapered Si core, and Ge_{0.9}Sn_{0.1} shell. The length and the pitch (u) of the Si core are $\sim 485 \text{ nm}$ and 500 nm , respectively (Fig. 1d). The core diameter increases toward the base from 20 nm to 120 nm (tapering angle of 6°). The refractive index of Si and Ge_{0.9}Sn_{0.1} thin film are measured with spectroscopic ellipsometry [25]. Next, the designed structure was built in two separate steps (Methods). The pitch was varied from 500 nm to $2 \mu\text{m}$. A scanning electron microscope (SEM) image of the metasurface and the corresponding electron energy loss spectroscopy (EELS) images of the Si, Ge, and Sn elements acquired using transmission electron microscopy (TEM) are displayed in Fig. 1e.

Rotating the incident light polarization from p - to s -state induces a clear reflectance enhancement from 5% to 17% at $1.734 \mu\text{m}$, as shown in Fig. 1c (indicated by the black arrow). This is equivalent to a transmission reduction from 50% to less than 5%, as simulated with

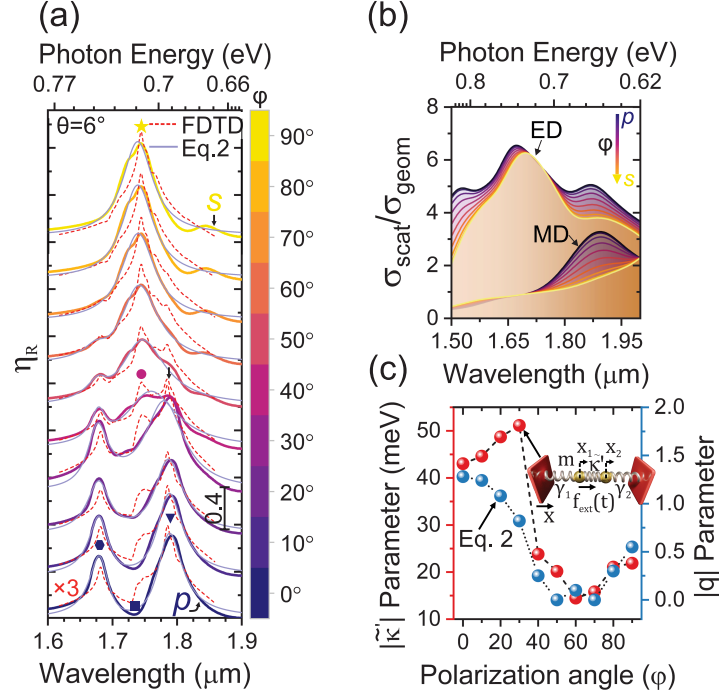


FIG. 2. **Light polarization and Fano resonance.** (a) Polarization-dependent reflectance ratio η_R characterization at a fixed AOI of 6° . The polarization is rotated from s -to p -state with a 10° step. The simulated FDTD specular reflectance ratio at each polarization is also overlaid in red-dashed traces. The theoretical model based on the lineshape fit (Eq. 3) is also shown as gray trace, whereas the CHO fit is shown in the Fig. S7. The different spectra are shifted upwards with 0.4 for clarity. The different markers are a visual reference for the near-field distribution that are analyzed in Fig. 3. (b) Scattering cross-section of the core/shell Si/Ge_{0.9}Sn_{0.1} NW as a function of the polarization. The ED and MD modes evolution vs. polarization angle ϕ is highlighted. (c) The evolution of the coupling parameter $|\kappa'|$ and the asymmetry parameter ($|q|$) as a function of ϕ evaluated respectively based on Eqs. 3 and 4. The inset shows a schematic of the mechanical coupled harmonic oscillator model used to simulate the PIR based on Eq. 4. Only the left oscillator is excited by the external force.

FDTD (Fig. S4). The Si core arrays were fabricated on single-side polished wafers, which prevents transmission measurements. Thus, reflectance (R) measurements are the focus of this study. The absorption measurements confirmed that the observed spectral features are emanating from the metasurface (Fig. S5). To study the optical reflectance of the core/shell NWs independently from the optical effects of the Si core, the ratio of the core/shell to that of the Si arrays $\eta_R = R_{\text{core/shell NW}}/R_{\text{Si NW}}$ is analyzed. Noticeably, the lineshape asymmetry is greatly affected by the polarization state of the incident light. The general lineshape of Fano-like resonances describes a broad variety of nanostructures [26]. To that end, polarization-dependent specular reflectance is analyzed to elucidate the physical mechanism of the PIR features, and the lineshape evolution. Fig. 2a details the ratio η_R at a fixed AOI of 6° where the electric field orientation is rotated from s to p polarization with a 10° step. As ϕ decreases from 90° to 0° , the reflectance peak at $1.74 \mu\text{m}$ is completely suppressed. Theoretical modeling is introduced to describe quantitatively the PIR response.

Theoretical Model. Polarization-dependent scattering cross-section simulations are undertaken for a single

Si/Ge_{0.9}Sn_{0.1} NW to reveal how light-matter interactions drive the PIR effect. A multipole expansion approach is performed using the theoretical method developed by Alaei *et al.* [27], where the impact of polarization on the multipole moments and their contributions to the total scattering cross-sections can be estimated. These multipole moments, computed using the electric field and the refractive index extracted from the 3D FDTD simulations, are used to evaluate the corresponding scattering cross-sections. Fig. 2b shows the evolution of the ED and MD moments as ϕ is gradually changed from p to s -state. The magnetic and electric quadrupole amplitudes are 13 and 4-fold smaller than their MD and ED counterparts, respectively (Fig. S6). Hence, the interference between the optically induced MD and ED is the driving force behind the observed PIR features. Additionally, as ϕ increases from 0° to 90° , the MD mode near $1.890 \mu\text{m}$ is completely suppressed, whereas the ED mode at $1.670 \mu\text{m}$ redshifts 25 nm, and a small mode near $1.890 \mu\text{m}$ still remains. It is important to highlight that the modal response has a Fano-like lineshape. This is confirmed by fitting the reflectance ratio η_R to a Fano-like asymmetric lineshape [26] (Figs. S7-S8).

A closed-form analytical formula [26] is used to extract the relevant PIR Fano parameters based on lineshape fitting (Eq. 3, Methods). Noticeably, Eq. 3 assumes $\omega_2 \gg \gamma_2$. Therefore, the Fano resonance results from the competition between the two dipoles, and the Fano lineshape heavily depends on the coupling between the relative dipole strengths. Consequently, the quantity q is a measure of this relative strength and, based on Fano's original theory [28], it can be expressed as:

$$q = \frac{1}{\pi L g} \times \frac{\mu_{\text{MD}}}{\mu_{\text{ED}}} \quad (1)$$

where L is the electromagnetic density of states at the ED resonance, g is the coupling strength between the ED and MD modes, and μ_{ED} and μ_{MD} are the total electric and magnetic moments. From Fig. 2b, the ED has a stronger moment than that of MD below 1.7 μm , which causes $|q| \approx 1$ and the asymmetrical Fano lineshapes become distinguishable at low polarization angle ($\varphi < 20^\circ$). The experimental and simulated data indicate that q is negative in our system (Table S1). The fitting curves are shown in Fig. 2a as gray traces. As φ increases from 30° to 90° , $|q|$ reaches a minimum value of 0 at 50° , and the asymmetrical lineshape becomes indistinguishable. The evolution of $|q|$, extracted from Eq. 3, as a function of the polarization angle (φ) is shown in Fig. 2c (blue circles). From Eq. 1, the Fano lineshape also depends on L and μ_{ED} of the ED resonance, and the coupling strength g . Therefore, changes to the metasurface geometry can tune the Fano lineshape asymmetry as well. To reveal how this works, we simulated the p -polarized specular reflectance at 6° AOI of different metasurfaces with variable bottom shell diameter d_{sB} (from 150 nm to 350 nm) and a fixed top shell diameter d_{sT} of 80 nm. The change in the lineshape asymmetry is evident as d_{sB} increases (Fig. S9). In fact, q increases from -1.76 to 0.30 , confirming the geometrical Fano resonance tunability.

To analyze the coupling strength g in the Si/GeSn metasurface, which is inaccessible with Fano's original formalism, we used the coupled harmonic oscillator (CHO) model to simulate the reflectance spectra [19, 29, 30]. The equivalent system shown in the inset of Fig. 2c is described by two coupled second-order differential equations, subject to an external source $f_{\text{ext}}(t)$ as indicated in Eq. 4 (Methods). The CHO models exceptionally well the Fano resonance (Fig. S7). The coupling coefficient $\tilde{\kappa}'$ parameter is, in principle, related to the coupling strength g in Eq. 1. Based on Fig. 2c (red circles), the ED and MD coupling parameter ($\tilde{\kappa}' \sim g$) show a clear drop from 50 meV to 25 meV at $\varphi = 40^\circ$, indicating a reduction in the transition dipole moments. Furthermore, the same qualitative trend is observed with the asymmetry parameter ($|q|$), where $|q|$ decreases from 1.28 to 0.25 to reach 0 at $\varphi = 50^\circ$. This confirms the direct relationship between the Fano resonance lineshape and the coupling strength, as stated in Eq. 1.

To evaluate near-field coupling around the PIR, the

near-field distributions ($|\mathbf{E}|^2, |\mathbf{H}|^2$) of the array are systematically analyzed at different polarization. Both electric and magnetic moments are highly polarization-dependant ($\cos \varphi$ and $\sin \varphi$ dependence respectively). Therefore, at the PIR, the ED and MD can be selectively enhanced. Fig. 3 shows the normalized near-field distributions at two different planes: $y = 0$ and $(x - y)$ for a NW unit cell at three different polarizations. Fig. 3a,b show the near-field distributions at the PIR mode, at 1.740 μm , whereas Fig. 3c at the (ED, MD) modes, at 1.678 μm and 1.790 μm respectively. First, the $(x - y)$ plane field distribution maps are shown at specific z values of the NW height. The heights are color-coded with the dashed traces in panel (a) for $|\mathbf{E}|^2$ at $\varphi = 90^\circ$ and for $|\mathbf{H}|^2$ at $\varphi = 0^\circ$. Second, a strong magnetic field localization at 1.740 μm is observed at the base of the NW when φ decreases from 90° to 0° . Third, in Fig. 3b, the normalized near-field distribution of the NW is analyzed near the base of the NW (Fig. 3b), at 1.740 μm for three polarization angles $\varphi = 0^\circ, 40^\circ$ and 90° . ED and MD are dominant at $\varphi = 0^\circ$, which is corroborated with the scattering cross-section calculations shown in Fig. 2b. When $\varphi = 90^\circ$, the electric field distribution shows an ED behavior with an enhanced field near the edges of the base, whereas the magnetic field $|\mathbf{H}|^2$ loses its MD character which is confirmed through the simulated large modal broadening near the base. Next, when $\varphi = 40^\circ$, MD and ED are equally excited and the near-field shows hybrid features. The nature of the electric and magnetic dipoles is well demonstrated in the $(x - y)$ cross-section maps of $|\mathbf{E}|^2$ at 1.678 μm and $|\mathbf{H}|^2$ at 1.790 μm (Fig. 3c), as the near-field shows typical dipole distribution in the top and middle region of the NW [31]. Near the base of the NW, the electric field is enhanced inside the Si core and the GeSn base edge, whereas the magnetic field is mainly confined inside the base of the NW. According to Fig. 3, the near-field distributions can be effectively manipulated by tuning the polarization of the incident light. The electric field can be selectively enhanced (Fig. 3b) at $\varphi = 0^\circ$ or suppressed at $\varphi = 90^\circ$ near the base of the NW. Thus, the electric and magnetic dipole interference remains polarization sensitive, which promotes the Fano resonance. For different polarizations, the ED and MD can also interfere simultaneously with the geometric resonance of the array through diffractive coupling thereby enhancing polarization-dependent Fano resonances.

To further inspect diffraction coupling effect on the PIR modes, period-dependent reflectance ratio of the core/shell metasurface is investigated. Three additional Si/GeSn arrays are fabricated with variable periods of 800 nm, 1 μm , and 2 μm as shown in the SEM images of Fig. S10. Given that only four periods are built, complementary FDTD simulations are undertaken for an increasing pitch length from 400 nm to 2 μm . Increasing the period induces a redshift and spectral broadening of the ED and MD modes up to 575 nm. This indicates that diffraction coupling to the dipole moments plays an important role in defining the width of the Fano resonance.

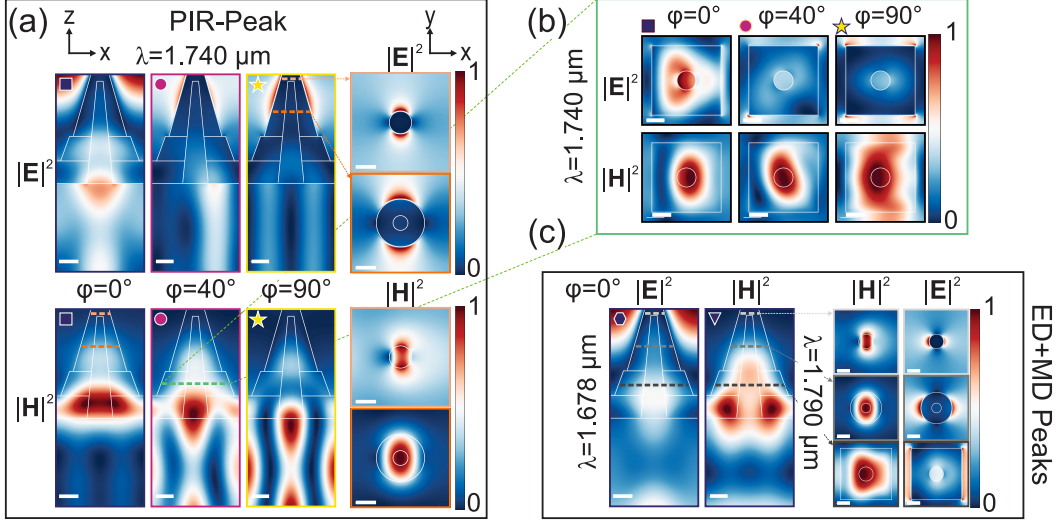


FIG. 3. **Effect of polarization on the near-field electric and magnetic distributions.** FDTD simulated electric and magnetic field distribution maps in the $y = 0$ and $(x - y)$ planes for the Si/GeSn array at specific spectral resonances: (a-b) at the polarization-induced reflectance dip located at $1.740 \mu\text{m}$ and (c) the ED and MD resonances, near $1.678 \mu\text{m}$ and $1.790 \mu\text{m}$, respectively. In (b), the effect of incident light polarization is investigated through a systematic description of the electric and magnetic field near only the base of the NW. The scale bar is set to 100 nm in all maps.

The combined effect of diffraction coupling and the Fano resonance asymmetry shapes the nature of the observed PIR. This finding lays the groundwork to exploit the NW metasurface in sensing applications, as demonstrated below.

Refractive index sensing. Due to the sharp Fano resonance between $1.60 \mu\text{m}$ and $1.9 \mu\text{m}$ and its polarization-enabled tunability, one promising application of these metasurfaces is optical sensing. The performance of RI sensing is typically evaluated by the FoM, defined as the ratio of the sensitivity (S) to the FWHM at the resonant peak [32],

$$\text{FoM} = \frac{S \text{ (nm/RIU)}}{\text{FWHM (nm)}} \quad (2)$$

The metasurface is immersed in a RI-matching oils (Methods) to supply different solutions with variable RI while the reflectance spectra are recorded at both s - and p -polarizations. Due to the strong interference of the ED and MD resonant modes, the Fano resonance mainly depends on the non-radiation damping, which makes it sensitive to the changes in the surrounding dielectric environment. Above all, the Fano mode exhibits a distinct resonance shift with respect to the small fluctuation in the RI of the surrounding medium ($\Delta n = 0.01$) (Fig. 4). Therefore, this offers an excellent potential for ultrahigh resolution required in bio-sensing and gas detection. Fig. 4a,b shows the normalized reflectance spectra for the Si/Ge_{0.9}Sn_{0.1} NW array as a function of variable RI, n from 1.40 to 1.45 at two distinct polarizations. According to Eq. 2, the sensitivity S is evaluated through the resonance wavelength shift over the RI change unit (RIU), while FoM takes

further consideration of the resonant lineshape [32]. The FWHM indicates the ability to confine electromagnetic fields at resonance mode, which set the sensing resolution. To get a consistent estimate for the FoM value, the FWHM are obtained from Eq. 3 and evaluated for each polarization angle, an FoM of 5.35 and 6.56 for the ED and MD modes, respectively at $\varphi = 0^\circ$. The FoM is around 8.0 at $\varphi = 90^\circ$. The ED and MD Q -factors are 57 and 40, respectively at $\varphi = 0^\circ$, whereas, at $\varphi = 90^\circ$, the Q -factor decreases to 30.5 due to the increase in the associated spectral width. The Q -factor is defined as $Q = \lambda/\Delta\lambda$, where $\Delta\lambda$ is the spectral width of the corresponding resonant mode. Fig. 4c shows a clear redshift of the Fano resonance peak, as well as the asymmetric ED and symmetric MD resonances with increasing RI. The sensitivity $S = \delta\lambda/\delta n$ (nm/RIU) of the metasurface is estimated through a linear fit of the peak position as a function of the RI. The sensitivity S is evaluated for both s and p polarizations. At $\varphi = 0^\circ$, the sensitivity associated to the ED and MD modes shifts are equal to 81 and 149 nm/RIU, respectively. The small sensitivity is directly related to the asymmetric nature of the Fano resonance, characterized by a negative q parameter (~ -2) (Table S1), when $\varphi = 0^\circ$. Next, at $\varphi = 90^\circ$, S increases in average 3-fold from the s - to the p -polarized incident light. To shed light on the performance of the RI sensor, a brief review of the preceding experimental all-dielectric RI sensors is presented in Table S2. Several characteristics distinguish the current work from the current state-of-the-art. The first is the polarization-dependent sensitivity S of the RI sensor. The second is the SWIR accessible spectral range, which cannot be covered by the reported platforms thus

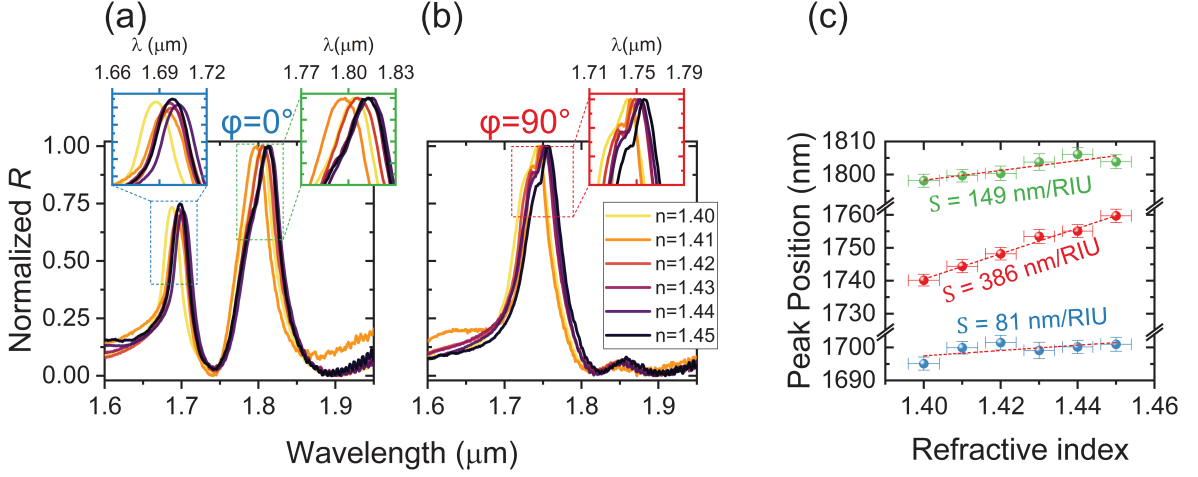


FIG. 4. **RI sensing results for the Si/Ge_{0.9}Sn_{0.1} array.** (a) Normalized reflectance spectra for different refractive index solutions from 1.40 to 1.45 at an incident light polarization of $\varphi = 0^\circ$. (b) Similar to panel (a) except the polarization angle φ is changed to 90° . The insets in both panels (a) and (b) are Zoom-in on the resonances showing the spectral shift in more detail. (c) Spectral shift of the resonances vs. RI of the surrounding solutions. Spheres are the experimental data points, extracted by fitting the indicated regions in panels (a) and (b), based on Eq. 3. The y-axis error bars indicate the uncertainty of the fitting process, with regards to the peak position, evaluated based on Eq. 3. The x-axis error bar is related to the uncertainty in the RI, evaluated based on the manufacturer RI quantification. The dashed red traces are linear fits to the data giving a sensitivity S of 149 nm/RIU and 81 nm/RIU for the PIR Fano resonance at a polarization angle φ of 0° and 389 nm/RIU when $\varphi = 90^\circ$. The R^2 of the linear regression is above 0.98.

far. Sensing devices operating in this spectral range are sought-after for both commercial and defense applications. The third is the achieved high sensitivity of 386 nm/RIU even though the Q -factor of the resonance is relatively low (30.5), when compared to early reports [33]. The observed increase in sensitivity is directly linked to the change in the asymmetry parameter q . Indeed, the more symmetric is the resonance mode, the higher is the sensitivity. In principle, any control of the Fano resonance features is driven by the geometric coupling that is accessible through micro-fabrication steps to enhance the sensing sensitivity. Although a metallic metamaterial has generally higher RI sensitivity than its all-dielectric counterparts, the former has smaller Q -factor than the latter. This directly affects the FoM of RI sensors.

In conclusion, we demonstrated the conformal growth of a 150 nm-thick metastable Ge_{0.9}Sn_{0.1} shell around tapered Si nanotips to establish a wafer-level, all-dielectric metasurface. We also presented a detailed discussion of its polarization-dependant specular reflectance. A rigorous theoretical analysis revealed that the interference between the ED and MD modes underlies the observed Fano resonance nature of the PIR. Additionally, the modulation of the Fano resonance by tuning the polarization is achieved by relating the asymmetry parameter of the Fano line-shape to the coupling strength between the ED and MD moments. To harness these polarization-tailored Fano resonances, a refractive index sensor is demonstrated using the fabricated metasurface. The sensitivity S of the proposed device reaches 386 nm/RIU at a polarization angle

of 90° , whereas at a 0° polarization, the ED- and MD-dependent sensitivity are 149 nm/RIU and 81 nm/RIU, respectively. It is possible to obtain a higher Q -factor and further improve the FoM by tuning only the tapered base dimensions, instead of the whole NW. This would simplify the design and fabrication of future metasurfaces. This platform can be easily integrated with microfluidic systems for lab-on-a-chip applications [34, 35]. Tunable Fano resonances in the SWIR range using all-dielectric metasurfaces pave the way to numerous applications ranging from nonlinear optics and sensing to the realization of new types of optical modulation and low-loss slow-light devices.

METHODS

Array Fabrication: Using a state-of-the-art pilot line for 130 nm SiGe BiCMOS technology, Si NW with diameters of 20-150 nm (top-bottom) were fabricated from a 300 mm Si(100) wafer by a multi-step procedure, including an anisotropic Ar:BCl₃:Cl₂-based reactive ion etching (RIE) process [36]. The Si NWs sample was then cleaned in an HF-based solution prior to loading in the low-pressure chemical vapor deposition (CVD) reactor. The GeSn shell was grown at 300 °C using ultra-pure H₂ carrier gas, and 10 % monogermane (GeH₄) and tin-tetrachloride (SnCl₄) precursors. A constant precursor supply with a GeH₄/SnCl₄ ratio of ~ 1700 was provided during the GeSn growth, hence with the same parameters as in the reference Ge_{0.90}Sn_{0.10} thin film layers grown on a Ge on Si substrate [37].

Optical Measurements: Polarization-resolved reflectance was acquired from 1 μm to 2.5 μm using a focused beam with a spectrophotometer. The wavelength was scanned at a step of 1 nm. The incident angle was varied between 6° and 52° with a step of 1° and the incident light polarization was changed between *s*- and *p*-states, as detailed by the schematic in Fig. 2a. A dispersion map of the metasurface was also measured (Fig. S2). The spot size was approximately 2.5 mm \times 2.5 mm, which covered approximately 20 million NWs. The wire grid polarizer was rotated from *s*- to *p*-polarized state with a 10° step. The NW metasurface was immersed in the refractive-index-matching oils (Cargille Labs) for all the sensing measurements. The samples were washed thoroughly after each measurement with isopropyl alcohol, dried with nitrogen gas, and followed by placing them in a vacuumed desiccator for 30 min to ensure that no residual oil was left after each measurement.

Simulations: The FDTD calculations are performed using Ansys-Lumerical® software. During the calculations, an electromagnetic pulse in the wavelength range from 1.1 to 2.5 μm is launched into a box containing the target core/shell NW to simulate a propagating plane wave interacting with the NW. The polarization type is defined with respect to the electromagnetic field orientation (*p*-type when the electric field is parallel to the surface, $\varphi = 0^\circ$, and *s*-type when the magnetic field is parallel to the surface, $\varphi = 90^\circ$). The Si/GeSn array and its surrounding space are divided into 5 nm meshes. The refractive index of the medium in the top and side regions is that of air ($n = 1$) and that in the bottom is set according to the dielectric functions of Si substrate. The refractive index of the silicon core is approximated to that of a Si substrate. A reference Ge_{0.9}Sn_{0.1} thin film was epitaxially grown to quantify both its real and imaginary dielectric function with spectroscopic ellipsometry [25]. A detailed structural characterization of the reference layer is shown in Fig. S11. The unit cell core/shell NW is modeled as two concentric frustums, as clearly highlighted in the scanning transmission electron microscopy (STEM) images (Fig. S3). Its dimensions are set to be the same as the average size measured from the SEM images. The different excitation polarizations are considered by setting the electric field in the substrate plane either parallel or perpendicular to the NW length axis, as well as being vertical to the substrate. Power monitors, positioned 100 nm below the air-Si interface and 500 nm above the NW, are used to determine the transmission and reflection at each wavelength, respectively. Perfectly matched layer (PML) boundary conditions are used in the vertical direction to prevent nonphysical scattering at the edge of the simulation box. When AOI = 0°, periodic boundary conditions are used in both in-plane dimensions to simulate an infinite periodic array, whereas Bloch boundary condition are considered when AOI > 0°. The field distributions are obtained according to the electric and magnetic field distributions at different resonance modes. They are calculated on the cross-sectional plane

that passes through the NW *z*-axis and perpendicular to the substrate (along *x*-*y* plane).

Scattering Calculation: The scattering-cross section simulations are performed using FDTD software (Ansys-Lumerical®) running on a 5 GHz workstation. The mesh size around the core/shell NW in the simulations is 5 \times 5 \times 5 nm³. The total-field/scattered-field (TFSF) plane wave is used as the excitation source, which leads to accurate evaluation of the scattered field outside the metasurface and the corresponding scattering cross section. PML boundary conditions are used to simulate an individual structure placed in an infinite space. The surrounding index in the simulations is vacuum with a refractive index $n = 1$.

Fitting Models: Two fitting models are considered in this work. First, a lineshape fitting approach is employed to extract the *Q*-factor, FWHM and mode resonance from the measured polarization-dependent reflectance ratio. The total reflectance $R(\omega)$ is expressed in the following form

$$R(\omega) = \frac{a^2}{\left(\frac{\omega^2 - \omega_1^2}{2\gamma_1\omega_1}\right)^2 + 1} \times \frac{\left(\frac{\omega^2 - \omega_2^2}{2\gamma_2\omega_2} + q\right)^2 + b}{\left(\frac{\omega^2 - \omega_2^2}{2\gamma_2\omega_2}\right)^2 + 1} \quad (3)$$

$\uparrow \qquad \qquad \qquad \uparrow$
 $R_1(\omega) \qquad \qquad \qquad R_2(\omega)$

The multipliers represent an interference between the radiation continuum and the ED mode throughout a symmetric Lorentzian lineshape $R_1(\omega)$ and the radiation continuum coupled to the MD mode through an asymmetric Fano-like lineshape $R_2(\omega)$. The asymmetric lineshape $R_2(\omega)$ describes the destructive or constructive interference due to the coherent coupling between the ED and MD modes. ω_1, γ_1 and ω_2, γ_2 are the resonant frequency and an approximation of the resonance spectral width of the ED and MD resonances, respectively. q is the Fano asymmetry parameter, b is the damping parameter originating from intrinsic losses, and a is the maximal amplitude of the resonance. Second, the CHO model is employed to quantify the coupling strength between the two modes. The fit is performed over the wavelength range from 1.6 μm to 1.9 μm , by solving the following coupled second-order differential equations,

$$\begin{aligned} \ddot{x}_1 + \gamma_1 \dot{x}_1 + \omega_1^2 x_1 + \tilde{\kappa}' \dot{x}_2 &= \alpha E_0 e^{i\omega t} |\cos \varphi|, \\ \ddot{x}_2 + \gamma_2 \dot{x}_2 + \omega_2^2 x_2 - \tilde{\kappa}' \dot{x}_1 &= 0, \end{aligned} \quad (4)$$

The first oscillator models the ED (radiative) mode with a frequency ω_1 and a damping γ_1 representing radiative losses. The second oscillator emulates the MD (nonradiative) with a resonant frequency ω_2 and a smaller damping γ_2 . The two oscillators coupling coefficient is $\tilde{\kappa}'$ and α is a parameter indicating the coupling strength of the radiative ED mode with the incident electromagnetic field $E_0 e^{i\omega t}$. A more elaborate discussion in relation to

the effect of the coupling strength on the reflectance ratio, is detailed in Fig. S8.

ACKNOWLEDGEMENTS

The authors thank J. Bouchard for the technical support with the CVD system, Brett Carnio with help with the Ansys-Lumerical[®] simulations, and C. Lemieux-Leduc for help with the Blender 3D schematic image in Fig. 1a. O.M. acknowledges support from NSERC Canada (Discovery, SPG, and CRD Grants),

Canada Research Chairs, Canada Foundation for Innovation, Mitacs, PRIMA Québec, and Defense Canada (Innovation for Defense Excellence and Security, IDEaS).

AUTHORS INFORMATION

Corresponding Authors:

*anis.attiaoui@polymtl.ca

† oussama.moutanabbir@polymtl.ca

Notes:

The authors declare no competing financial interest.

-
- [1] P. Fan, Z. Yu, S. Fan, and M. L. Brongersma, *Nature Materials* **13**, 471 (2014).
 - [2] M. F. Limonov, M. V. Rybin, A. N. Poddubny, and Y. S. Kivshar, *Nature Photonics* **11**, 543 (2017).
 - [3] R. Sarma, N. Nookala, K. J. Reilly, S. Liu, D. de Ceglia, L. Carletti, M. D. Goldflam, S. Campione, K. Sapkota, H. Green, G. T. Wang, J. Klem, M. B. Sinclair, M. A. Belkin, and I. Brener, *Nano Lett.* **21**, 367 (2021).
 - [4] J. C. Ginn, I. Brener, D. W. Peters, J. R. Wendt, J. O. Stevens, P. F. Hines, L. I. Basilio, L. K. Warne, J. F. Ihlefeld, P. G. Clem, and M. B. Sinclair, *Physical Review Letters* **108**, 097402 (2012).
 - [5] P. Moitra, Y. Yang, Z. Anderson, I. I. Kravchenko, D. P. Briggs, and J. Valentine, *Nature Photonics* **7**, 791 (2013).
 - [6] S. Linden, C. Enkrich, M. Wegener, J. Zhou, T. Koschny, and C. M. Soukoulis, *Science* **306**, 1351 (2004).
 - [7] C. Enkrich, M. Wegener, S. Linden, S. Burger, L. Zschiedrich, F. Schmidt, J. F. Zhou, T. Koschny, and C. M. Soukoulis, *Physical Review Letters* **95**, 203901 (2005).
 - [8] C. M. Soukoulis and M. Wegener, *Nature Photonics* **5**, 523 (2011).
 - [9] J. Zhou, T. Koschny, M. Kafesaki, E. N. Economou, J. B. Pendry, and C. M. Soukoulis, *Physical Review Letters* **95**, 223902 (2005).
 - [10] F. He, B. Han, X. Li, T. Lang, X. Jing, and Z. Hong, *Optics Express* **27**, 37590 (2019).
 - [11] F. Hao, Y. Sonnefraud, P. V. Dorpe, S. A. Maier, N. J. Halas, and P. Nordlander, *Nano Letters* **8**, 3983 (2008).
 - [12] F. Zhang, X. Hu, Y. Zhu, Y. Fu, H. Yang, and Q. Gong, *Applied Physics Letters* **102**, 181109 (2013).
 - [13] W. Zhu, Y. Fan, C. Li, R. Yang, S. Yan, Q. Fu, F. Zhang, C. Gu, and J. Li, *Nanoscale* **12**, 8758 (2020).
 - [14] Y. Zhang, C. Fowler, J. Liang, B. Azhar, M. Y. Shalaginov, S. Deckoff-Jones, S. An, J. B. Chou, C. M. Roberts, V. Liberman, M. Kang, C. Ríos, K. A. Richardson, C. Rivero-Baleine, T. Gu, H. Zhang, and J. Hu, *Nature Nanotechnology* **16**, 661 (2021).
 - [15] Y. Meng, Y. Chen, L. Lu, Y. Ding, A. Cusano, J. A. Fan, Q. Hu, K. Wang, Z. Xie, Z. Liu, Y. Yang, Q. Liu, M. Gong, Q. Xiao, S. Sun, M. Zhang, X. Yuan, and X. Ni, *Light: Science & Applications* **10**, 235 (2021).
 - [16] H.-T. Chen, A. J. Taylor, and N. Yu, *Reports on Progress in Physics* **79**, 076401 (2016).
 - [17] I. Staude and J. Schilling, *Nature Photonics* **11**, 274 (2017).
 - [18] A. Krasnok, M. Tymchenko, and A. Alù, *Mater. Today* **21**, 8 (2018).
 - [19] B. Luk'yanchuk, N. I. Zheludev, S. A. Maier, N. J. Halas, P. Nordlander, H. Giessen, and C. T. Chong, *Nature Materials* **9**, 707 (2010).
 - [20] W. Cao, R. Singh, I. A. I. Al-Naib, M. He, A. J. Taylor, and W. Zhang, *Optics Letters* **37**, 3366 (2012).
 - [21] P. Offermans, M. C. Schaafsma, S. R. K. Rodriguez, Y. Zhang, M. Crego-Calama, S. H. Brongersma, and J. Gómez Rivas, *ACS Nano* **5**, 5151 (2011).
 - [22] Y. Yang, W. Wang, A. Boulesbaa, I. I. Kravchenko, D. P. Briggs, A. Poretzky, D. Geohegan, and J. Valentine, *Nano Lett.* **15**, 7388 (2015).
 - [23] Y. Hu, X. Wang, X. Luo, X. Ou, L. Li, Y. Chen, Ping Yang, S. Wang, and H. Duan, *Nanophotonics* **9**, 3755 (2020).
 - [24] O. Moutanabbir, S. Assali, X. Gong, E. O'Reilly, C. A. Broderick, B. Marzban, J. Witzens, W. Du, S.-Q. Yu, A. Chelnokov, D. Buca, and D. Nam, *Applied Physics Letters* **118**, 110502 (2021).
 - [25] A. Attiaoui, E. Bouthillier, G. Daligou, A. Kumar, S. Assali, and O. Moutanabbir, *Physical Review Applied* **15**, 014034 (2021).
 - [26] B. Gallinet and O. J. F. Martin, *Physical Review B* **83**, 235427 (2011).
 - [27] R. Alaee, C. Rockstuhl, and I. Fernandez-Corbaton, *Optics Communications* **407**, 17 (2018).
 - [28] U. Fano, *Physical Review* **124**, 1866 (1961).
 - [29] C. L. Garrido Alzar, M. A. G. Martinez, and P. Nussenzeig, *American Journal of Physics* **70**, 37 (2002).
 - [30] D. M. Riffe, *Physical Review B* **84**, 064308 (2011).
 - [31] C. F. Bohren and D. R. Huffman, *Absorption and Scattering of Light by Small Particles* (Wiley, New York, NY, 1998) p. 530.
 - [32] L. J. Sherry, S.-H. Chang, G. C. Schatz, R. P. Van Duyne, B. J. Wiley, and Y. Xia, *Nano Letters* **5**, 2034 (2005).
 - [33] Y. Yang, I. I. Kravchenko, D. P. Briggs, and J. Valentine, *Nature Communications* **5**, 5753 (2014).
 - [34] F. Peyskens, A. Dhakal, P. Van Dorpe, N. Le Thomas, and R. Baets, *ACS Photonics* **3**, 102 (2016).
 - [35] C. Chen, D. A. Mohr, H.-K. Choi, D. Yoo, M. Li, and S.-H. Oh, *Nano Lett.* **18**, 7601 (2018).
 - [36] O. Skibitzki, I. Prieto, R. Kozak, G. Capellini, P. Zaumseil, Y. Arroyo Rojas Dasilva, M. D. Rossell, R. Erni, H. von Känel, and T. Schroeder, *Nanotechnology* **28**, 135301 (2017).
 - [37] S. Assali, J. Nicolas, and O. Moutanabbir, *Journal of Applied Physics* **125**, 025304 (2019).